The Astrophysical Journal, 966:106 (15pp), 2024 May 1 https://doi.org/10.3847/1538-4357/ad35cb

Empirical Models of the Hβ Broad Emission Line Gas Density Field

Lizvette Villafaña[1], Tommaso Treu[1], Lourenzo Colleyn[1], Brendon J. Brewer[2], Aaron J. Barth[3], Matthew A. Malkan[1], Vivian U[3], and Vardha N. Bennert[4]
[1] Department of Physics and Astronomy, University of California, Los Angeles, Los Angeles, CA 90095-1547, USA; lvillafana@astro.ucla.edu
[2] Department of Statistics, The University of Auckland, Private Bag 92019, Auckland 1142, New Zealand
[3] Department of Physics and Astronomy, 4129 Frederick Reines Hall, University of California, Irvine, Irvine, CA 92697, USA
[4] Physics Department, California Polytechnic State University, San Luis Obispo, CA 93407, USA
Received 2024 February 7; revised 2024 March 16; accepted 2024 March 18; published 2024 April 29

Abstract

We present the second iteration of the CARAMEL-GAS code, an empirical model of the broad-line region (BLR) gas density field. Building on the initial development and testing of CARAMEL-GAS, we expand the meaning of the model parameter α, which initially represented only the power-law index of the dependency of emissivity on radial distance. In this work, we test a more generalized radial power-law index, α, that also includes a description of the effective emitting size(s) of the BLR structure as a function of radial distance. We select a sample of 10 active galactic nuclei (AGN) from three different Lick AGN Monitoring Project campaigns to further validate the CARAMEL-GAS code and test the generalized radial power-law index, α. Our results confirm that the CARAMEL-GAS results are in general agreement with the published results determined using the original CARAMEL code, further demonstrating that our forward modeling method is robust. We find that a positive radial power-law index is generally favored and propose three possible scenarios: (i) the BLR structure has increasing effective emitting size(s) at larger radial distances from the central source, (ii) emission is concentrated at the outer edges of the BLR, and (iii) stronger theoretical assumptions are needed to break the degeneracies inherent to the interpretation of reverberation mapping data in terms of underlying gas properties.

Unified Astronomy Thesaurus concepts: Active galactic nuclei (16); Active galaxies (17); Supermassive black holes (1663)

1. Introduction

While the standard model of active galactic nuclei (AGN) provides a well-developed framework that explains the different AGN features observed (Antonucci 1993; Urry & Padovani 1995; Urry 2003), details of the different components, such as the structure and dynamics, still remain uncertain (for a review, see Netzer 2015). Understanding the structure and behavior of gas near the vicinity of the central engine is of great interest, as such insight may help us better understand the role AGN play in galaxy evolution (Booth & Schaye 2009; Fabian 2012; Somerville & Davé 2015; Dubois et al. 2016). Given that the broad-line region (BLR) is the closest structure, of order of ∼light-days for low-luminosity AGN (Kaspi et al. 2000), to the central black hole, the BLR has been the focus of a wide range of AGN astrophysics studies.

From a theoretical standpoint, several scenarios of the BLR gas have been proposed, ranging from discrete clouds (Krolik 1988; Rees et al. 1989; Baldwin et al. 1995), to bloated stars (Scoville & Norman 1988) and comets (Maiolino et al. 2010), to perhaps the most recently favored, disk winds (Emmering et al. 1992; Murray et al. 1995; Elvis et al. 2002; for a review, see Peterson 2006, and references therein). From an observational standpoint, the BLR cannot be spatially resolved, and most information known about the BLR involves resolving the BLR in time using the technique of reverberation mapping (but see, however, Gravity Collaboration et al. 2018, 2020, 2021, for recent breakthroughs through the use of interferometry).

Reverberation mapping campaigns involve intensive photometric and spectroscopic observations over the course of several months, in order to observe variations in the ionizing continuum reverberate as variations in the broad emission line fluxes at a later time, τ (Blandford & McKee 1982; Peterson 1993; Peterson et al. 2004; for a more recent review, see Cackett et al. 2021). This technique has proven very valuable in calibrating over 70 AGN black hole masses (see Bentz & Katz 2015, for details regarding their online AGN black hole mass database).

In principle, one can map how changes in the continuum translate to changes in the broad emission line fluxes as a function of line-of-sight (LOS) velocity and time delay, i.e., the transfer function, to learn more about the structure and kinematics of the BLR (Peterson 1993), although interpretation is not straightforward and requires additional modeling (Horne 1994; Cackett & Horne 2006). As an alternative approach, our team pioneered the method of forward modeling reverberation mapping data sets using the Code for AGN Reverberation and Modeling of Emission Lines (CARAMEL). The BLR Reverberation-mapping Analysis In AGNs with Nested Sampling code by Li et al. (2013) also follows a similar forward modeling approach, and the Broad Emission Line Mapping Code by Rosborough et al. (2023) may be modified in the near future to include forward modeling capabilities.

Using high-quality reverberation mapping data sets, we have modeled the BLR *emission* for over 28 AGN (Pancoast et al. 2014; Grier et al. 2017; Williams et al. 2018, 2020; Bentz et al. 2021a, 2022, 2023a, 2023b; Villafaña et al. 2022). While this original version of the code sufficiently models various aspects

of BLR geometry and kinematics, e.g., disk inclination, disk thickness, inflow/outflow behavior, the BLR is modeled as a collection of point particles near a central ionizing source that instantaneously reemit absorbed power. For this reason, CARAMEL only models the emissivity distribution, rather than the actual underlying gas distribution, and we interpret the BLR model as a Monte Carlo representation of the emissivity field. We will refer to this original version of the code, which models the BLR emissivity field, as CARAMEL-LIGHT throughout the rest of the paper.

Williams & Treu (2022, hereafter W22) modified CARAMEL-LIGHT to include a simple power law that connects the observed BLR emission to the underlying gas distribution in a version of the code we now call CARAMEL-GAS. In this way, CARAMEL-GAS models the BLR as a Monte Carlo representation of the gas density field, rather than the emissivity field. A representation of the gas density field would prove to be an advantage for fitting multiple emission lines at once, e.g., Hα and Hβ or C III and C IV. With the current version of the code, however, emission lines must be modeled individually and can only be compared a posteriori (Williams et al. 2020; W22). Future development to incorporate the ability to model multiple emission lines requires additional testing and understanding of the capabilities of CARAMEL-GAS—which is the focus of this paper.

The resulting gas density field produced by CARAMEL-GAS can be interpreted through the lens of different theoretical scenarios, such as BLR clouds or a continuous disk wind structure. While we believe that more recent developments in the theory may be pointing toward the latter (Waters et al. 2016; Mangham et al. 2017; Waters & Li 2019), we will often refer to the BLR as "clouds" throughout this paper, for the sake of our argument as we consider all possible interpretations. Therefore, we want to emphasize that our use of this terminology does *not* mean that the BLR cloud model is our preferred interpretation. In particular, we would like the reader to keep in mind that CARAMEL-GAS models the BLR gas as a Monte Carlo representation of the gas density field, and although we may often refer to the BLR as discrete clouds, this is only one possible interpretation that we include for completeness.

Our work builds on the initial development and testing stage of CARAMEL-GAS, in which W22 found the emissivity power-law index, α—the new model parameter that relates observed emission to the gas distribution—pushing up against its prior of -2 to 0, suggesting a preference for positive values. W22 speculated whether the assumption of point particles, which are used to represent the gas density field, with equal emitting size contributed to these results. Using the interpretation of discrete clouds and pressure law models (Rees et al. 1989), W22 proposed including an additional radial power-law index, $\alpha_{\rm size}$, that allows for varying size(s) of the BLR structure/clouds as a function of radial distance from the central black hole. In this paper, we use a sample of 10 AGN to further validate the CARAMEL-GAS code and test a new general form of the radial power-law index, which includes both an emissivity power-law index and a size power-law index for the BLR structure/clouds.

We outline our sample selection in Section 2, and we briefly summarize CARAMEL-LIGHT, the first implementation of CARAMEL-GAS, and the additional modifications applied to CARAMEL-GAS for this work in Section 3. We present our results and discuss possible interpretations of a positive power-law index, α, in Section 4, and we conclude in Section 5.

2. Sample Selection

Due to the computational power required for any CARAMEL modeling, we choose to limit the number of AGN to model using CARAMEL-GAS. While a total of at least 28 AGN have been modeled using CARAMEL-LIGHT (see Villafaña et al. 2022, for a recent list), we use only those observed during the Lick AGN Monitoring Project (LAMP) campaigns—LAMP 2008 (Bentz et al. 2009; Walsh et al. 2009), LAMP 2011 (Barth et al. 2011, 2015), and LAMP 2016 (U et al. 2022)—due to homogeneous data reduction and analyses.

In order to determine the sample of AGN to model using CARAMEL-GAS, we use two Hβ variability statistics that are standard in reverberation mapping analyses, $F_{\rm var}$ and $R_{\rm max}$. The variability statistic $R_{\rm max}$ refers to the ratio of maximum to minimum flux, and the noise-corrected fractional variation, $F_{\rm var}$, is computed as

$$F_{\rm var} = \frac{\sqrt{\sigma^2 - \delta^2}}{\langle F \rangle}, \tag{1}$$

where σ^2 is the variance of the fluxes, δ^2 is their mean square uncertainty, and $\langle F \rangle$ is the mean flux.

We compile the variability statistics from the original reverberation mapping analyses of our sample and tabulate them in Table 1. To focus on objects having high-quality reverberation mapping data, we select targets from LAMP campaigns that exhibited fractional variability amplitude $F_{\rm var} \geqslant 0.1$ and ratio of maximum to minimum flux $R_{\rm max} \geqslant 0.4$ in the integrated Hβ light curves (see Figure 1). While the quality of reverberation mapping data additionally depends on light-curve cadence, duration, and signal-to-noise ratio, these variability criteria effectively reject the LAMP data sets with lower variability amplitudes that are not suitable for velocity-resolved line profile modeling. We note that Mrk 50 (LAMP 2011), NGC 4593 (LAMP 2011), and Arp 151 (LAMP 2008) were previously modeled with CARAMEL-GAS during the initial development and testing was done by W22. However, we include these three AGN in our sample since one of our goals is to test a more generalized radial power-law index, α, and these three AGN were modeled during the CARAMEL-GAS development phase using the original parameter α, which did not include a radial power-law index for the reflecting surface area(s) of the BLR structure/clouds (please see Section 3 for a further discussion).

For our selected sample, we use the spectral decompositions originally used for CARAMEL-LIGHT and model the same wavelength ranges (see Table 2) for each AGN. For details regarding the spectral decompositions of the reverberation mapping data sets, we refer the reader to the original CARAMEL-LIGHT work of a given AGN, which can also be found in Table 2. The spectra used for the original CARAMEL-LIGHT modeling have flux or magnitude units. As we will discuss later in Section 3.5, CARAMEL-LIGHT does not fit absolute fluxes and instead includes a scaling factor to match the continuum and emission-line strengths. In CARAMEL-GAS, we fit the absolute fluxes by scaling the continuum light curves and emission lines to luminosity units using the luminosity distances found in Table 2. Conversion of spectral units required for CARAMEL-GAS modeling will be further discussed in Section 3.

Table 1
LAMP AGN Hβ Variability Statistics

Campaign and Corresponding CARAMEL-LIGHT	Galaxy	Redshift	$F_{\rm var}$; Reference	$R_{\rm max}$; Reference	Selected?
Lick AGN Monitoring Project (LAMP 2008; Pancoast et al. 2014, hereafter P14)	Arp 151	0.02109	0.169; (1)	1.74 ± 0.04; (1)	Yes*
	Mrk 1310	0.01941	0.108; (1)	1.62 ± 0.04; (1)	Yes
	NGC 5548	0.01718	0.082; (1)	1.57 ± 0.35; (1)	No
	NGC 6814	0.00521	0.093; (1)	1.58 ± 0.11; (1)	No
	SBS 1116+583A	0.02787	0.102; (1)	1.48 ± 0.06; (1)	Yes
Lick AGN Monitoring Project (LAMP 2011; Williams et al. 2018, hereafter W18)	Mrk 141	0.04170	0.080; (2)	1.39 ± 0.03; (2)	No
	Mrk 1511	0.03390	0.120; (2)	1.42 ± 0.03; (2)	Yes*
	Mrk 279	0.03050	0.070; (2)	1.31 ± 0.01; (2)	No
	Mrk 50	0.02340	0.200; (2)	2.17 ± 0.13; (2)	Yes*
	NGC 4593	0.00900	0.230; (2)	2.11 ± 0.08; (2)	Yes
	PG 1310-108	0.03430	0.050; (2)	1.29 ± 0.02; (2)	No
	Zw 229-015	0.02790	0.250; (2)	2.81 ± 0.07; (2)	Yes
Lick AGN Monitoring Project (LAMP 2016; Villafaña et al. 2022, hereafter V22)	MCG +04-22-042	0.03235	0.268; (3)	0.95; (3)	Yes
	Mrk 1048	0.04314	0.071; (3)	0.62; (3)	No
	Mrk 1392	0.03614	0.173; (3)	0.95; (3)	Yes
	Mrk 841	0.03642	0.073; (3)	0.74; (3)	No
	NPM1G +27.0587	0.06200	0.051; (3)	0.74; (3)	No
	PG 2209+184	0.07000	0.122; (3)	0.89; (3)	Yes
	RBS 1303	0.04179	0.081; (3)	0.90; (3)	No
	RBS 1917	0.06600	0.028; (3)	0.76; (3)	No
	RXJ 2044.0+2833	0.05000	0.055; (3)	0.78; (3)	No

Note. We select our sample for this work from the sources modeled with CARAMEL-LIGHT from the three different LAMP campaigns—LAMP 2008, LAMP 2011, LAMP 2016. Column (1) specifies the campaign from which the data were collected and the corresponding CARAMEL-LIGHT paper. The galaxy name and redshifts are found in Columns (2) and (3), respectively. Redshifts are from the NASA/IPAC Extragalactic Database (NED). The Hβ variability statistics—noise-corrected fractional variation, $F_{\rm var}$, and the ratio of maximum to minimum flux, $R_{\rm max}$—are found in Columns (4) and (5), respectively. We require $F_{\rm var} > 0.1$ and $R_{\rm max} > 0.4$ when selecting our sample. Column (6) shows whether the AGN was selected for our sample or not. "Yes*" signifies that the AGN selected has previously been modeled using CARAMEL-GAS, during the initial implementation and testing phase (W22).
References. (1) Bentz et al. 2009; (2) Barth et al. 2015; (3) U et al. 2022.

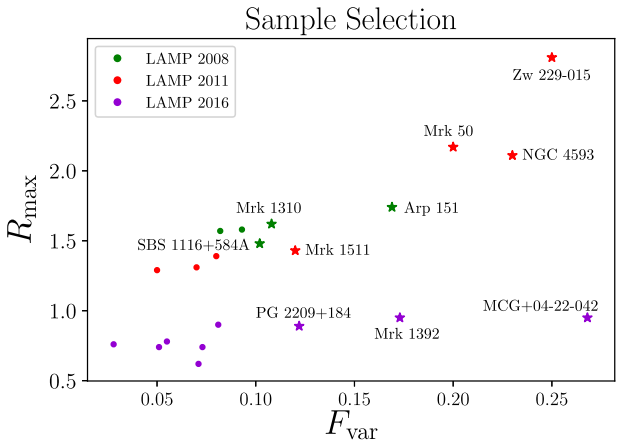

Figure 1. We select our sample from data collected during the three observation campaigns: LAMP 2008 (shown in green), LAMP 2011 (shown in red), and LAMP 2016 (shown in purple). We compare the Hβ variability statistics $R_{\rm max}$ and $F_{\rm var}$ to select our sample. The AGN shown in the plot above represent only the 21 LAMP AGN that have successful CARAMEL-LIGHT modeling. More AGN were observed during each campaign, but we do not include those with insufficient data quality for CARAMEL modeling. Our selection criteria require $F_{\rm var} \geqslant 0.1$ and $R_{\rm max} \geqslant 0.4$. In total, we select 10 AGN for CARAMEL-GAS modeling, which are depicted with a star marker above.

3. The Model

We begin with a brief description of the original CARAMEL-LIGHT model, followed by the modifications implemented by W22 to create CARAMEL-GAS. We then discuss additional modifications made to CARAMEL-GAS in this work and the modeling details for the 10 AGN presented here, as well as the model degeneracies we might expect to find with CARAMEL-GAS.

3.1. Overview of CARAMEL-LIGHT

For a full overview of CARAMEL-LIGHT, please see P14. In summary, CARAMEL-LIGHT models the BLR *emission* by sampling a distribution of point particles surrounding a central black hole located at the origin. The model assumes that the central engine (the black hole) is the ionizing source and that the BLR particles instantaneously reprocess and reemit the model continuum. In this way, the particles represent a Monte Carlo realization of the emissivity field, rather than the actual BLR gas distribution.

Utilizing a Bayesian framework, CARAMEL-LIGHT uses a diffusive nested sampling code, DNEST4 (Brewer & Foreman-Mackey 2018), to explore a 27-parameter space and infer the model parameters that best fit the reverberation mapping data set. To account for systematic uncertainty from using a simple model, DNEST4 uses a statistical temperature, T, to weigh the likelihood when calculating the posterior, i.e., $\log(\text{posterior}) \propto \log(\text{prior}) + \log(\text{likelihood})/T$. The use of this likelihood softening parameter, T, corresponds to inflating the error bars by $\sqrt{T}$, and the value of T is selected post-analysis such that parameters converge in a smooth and unimodal fashion (Bentz et al. 2021b).

Table 2
AGN CARAMEL-GAS Modeling Properties

Campaign	Galaxy	Photometry	D_L (Mpc)	Hβ Wavelength (Å)	Intrinsic [O III] Width (Å)	R_0; Reference (lt-day)	T
LAMP 2008 (P14)	Arp 151	B^*	94.8	[4893.4, 5037.4]	1.562 ± 0.071	4.08; (1)	65
	Mrk 1310	B^*	87.1	[4909, 5007]	0.0852 ± 0.071	3.74; (1)	50
	SBS 1116+583A	B^*	125.8	[4931, 5061]	1.4 ± 0.3	2.38; (1)	30
LAMP 2011 (W18)	Mrk 1511	V	153.8	[4920, 5129]	1.7 ± 1.5	5.44; (2)	200
	Mrk 50	V	106.7	[4900, 5049]	1.7 ± 1.5	8.66; (2)	130
	NGC 4593	V	40.1	[4840, 4958]	1.8 ± 0.1	3.52; (3)	175
	Zw 229-015	V	126.0	[4890, 5048]	2.12 ± 0.1	5.9; (3)	50
LAMP 2016 (V22)	MCG +04-22-042	V	150.7	[4945, 5115]	2.08 ± 1.5	13.7; (4)	70
	Mrk 1392	V	164.2	[4845, 5180]	2.08 ± 1.5	27.6; (4)	270
	PG 2209+184	V	325.8	[5080, 5356]	2.08 ± 1.5	14.6; (4)	70

Note. Column (1) specifies the campaign from which data were collected and the corresponding CARAMEL-LIGHT modeling. The name of the galaxy is found in Column (2), and Column (3) specifies the photometric band used for the continuum light curve. Those denoted with an asterisk were measured using magnitudes, and the rest were measured in flux density units f_λ in 10^{-15} erg cm^{-2} s^{-1} Å^{-1}. For the continuum light curves given in units of magnitude, light curves were first converted to flux density units before being converted into luminosity units (see Section 4). We use the luminosity distances tabulated in Column (4) to convert continuum and Hβ light curves from flux density units to luminosity units. Luminosity distances were calculated by adopting $H_0 = 67.8$ km s^{-1} Mpc^{-1}, $\Omega_m = 0.308$, and $\Omega_{\rm vac} = 0.692$ (Planck Collaboration et al. 2016), in order to remain consistent with previous CARAMEL-LIGHT work. Column (5) represents the wavelength ranges modeled (in the observed frame), which were chosen to match the window selections used in the AGN's original CARAMEL-LIGHT modeling. Column (6) is the intrinsic [O III] λ5007 line width used, also selected to match the original values used for CARAMEL-LIGHT modeling. Column (7) is the pivot radius determined by the cross-correlation time lag measurement, $\tau_{\rm cent}$ (in the observed frame). Finally, Column (8) is the statistical temperature used to account for systematic uncertainty from using a simple model (see Section 3 for discussion).
References. (1) Bentz et al. 2009; (2) W22; (3) W18; (4) U et al. 2022.

We note two potential limitations with this simplified model. First, disk-outflow models suggest that the BLR and the obscuring torus may form one continuous structure that feeds/flows from the central accretion disk (e.g., Emmering et al. 1992; Konigl & Kartje 1994; Kartje & Königl 1996; Kishimoto et al. 2011; Koshida 2015). Since we model the central engine as the ionizing source, our model is incompatible with disk-outflow models and cannot provide information about the accretion disk. Additionally, we assume that gravity is the dominant force and do not take into account radiation pressure. This can lead to biased results for sources with high Eddington ratio AGN. However, LAMP sources have been found to have moderate Eddington ratios in prior studies (V22).

3.1.1. Modeling the Emission Line

In principle, any broad emission line can be used for modeling. Here we model only the Hβ emission line for our sample of low-redshift galaxies. We note that our team's primary future goal with the development and testing of CARAMEL-GAS is to model multiple emission lines simultaneously, for a given object. In particular, we would like to model the full extent of the BLR at once, using physically motivated emissivity profiles for different emission lines that originate from different BLR radial zones. Current reverberation mapping data sets that cover multiple emission lines include NGC 5548 (De Rosa et al. 2015) and Mrk 817 (Kara et al. 2021).[5] To realize our goal of modeling multiple emission lines simultaneously, however, additional testing of CARAMEL-GAS is required first—which is the focus of this paper.

In addition to data regarding the emission line being modeled, CARAMEL-LIGHT utilizes the V/B-band continuum light curve measured from the photometric campaign since it serves as a proxy for the ionizing continuum. CARAMEL-LIGHT uses Gaussian processes to model the continuum light curve, in order to interpolate between data points and evaluate the flux of the ionizing source at any arbitrary time. This allows the emission line, which echoes the variations of the ionizing source, to be modeled at any arbitrary time using the BLR particle distribution determined by the CARAMEL-LIGHT model parameters.

The radial distribution of the particles around the central source is described by a shifted gamma distribution, and a change of variables is computed so that the radial distribution is described by the model parameters μ, β, and F. The parameter μ represents the mean value of the shifted gamma distribution, the parameter β represents the standard deviation of the shifted gamma distribution, and the parameter F represents the fraction of μ from the origin where the shifted gamma distribution begins. In addition to these three parameters, the radial distance, r_i, of a particle is also defined by the Schwarzschild radius, which determines the lower limit for particle positions as measured from the central black hole. The effects of the model parameters μ and β on the radial distribution of particles will be further discussed in Section 3.6.

Once the particles are placed around the central black hole, according to the shifted gamma distribution and model parameters μ, β, and F described above, the particle position determines the time lag of the particle, τ_i, or how long the particle takes to reverberate variations in the continuum. Assuming that observed time delays are due to light-travel time, as done with traditional reverberation mapping analyses, the value of τ_i simply corresponds to the particle's distance from the origin divided by the speed of light, $\tau_i = r_i/c$. Then, for a given particle i, the LOS velocity determines the wavelength emitted, i.e., how much it is shifted from the rest wavelength of the emission line.

The model then determines the amplitude of the emission line using the amplitude, $C(t - \tau_i)$, of the continuum light curve

[5] For comparison of NGC 5548 Lyα, Hβ, and C IV CARAMEL-LIGHT BLR models, done a posteriori, see Williams et al. (2020).

at a time $t-\tau_i$ and allows for additional rescaling of the emission-line amplitude via model parameters ξ, κ, $C_{\rm mult}$, and $C_{\rm add}$. The parameter ξ describes the BLR midplane transparency and represents the fraction of particles emitting from the "far" side of the BLR and ranges from 0 to 1. The parameter κ ranges from -0.5 to 0.5 and is related to the relative brightness of each particle. The emission of each particle is weighted by $W = 0.5 + \kappa\cos(\phi)$, where ϕ is the angle between the particle's LOS to the origin (ionizing source) and the observer's LOS to the origin. Positive values of κ represent preferential emission away from the ionizing source, and negative values of κ represent preferential emission toward the ionizing source.

To understand the free parameters $C_{\rm mult}$ and $C_{\rm add}$, it is important to note that the absolute fluxes of both the continuum and the emission line are not modeled in CARAMEL-LIGHT. Instead, the fluxes are rescaled so that they are in units of order unity. Since the continuum fluxes used in the model are not absolute, the free parameters $C_{\rm mult}$ and $C_{\rm add}$ are multiplicative and additive factors included to match the overall amplitude (via $C_{\rm mult}$) and amplitude of variations (via $C_{\rm add}$) of the data. Combining all these factors, the line emission for a particle i at time t is calculated in the model using the following equation:

$$L_i(t) = W(\xi, \phi_i, \kappa)C_{\rm mult}[C(t-\tau_i) + C_{\rm add}], \quad (2)$$

where $L_i(t)$ is the line emission of particle i at time t, $C(t)$ is the observed continuum at time t, $C(t-\tau_i)$ is the observed continuum that arrives at the particle at time t given its distance and associated time lag τ_i, $C_{\rm mult}$ is the multiplicative factor included to match the overall amplitude of the data, $C_{\rm add}$ is the additive factor included to match the amplitude of variations of the data, and $W(\xi, \phi_i, \kappa)$ is a weighting function determined by the model parameters ξ and κ.

Once the amplitude of the emission line emitted by each particle is determined using Equation (2) above, the wavelength of the emission line emitted from each particle is determined by the particle's LOS velocity. The total emission line is then found by summing the contribution from each particle.

Finally, to account for instrumental resolution, we blur the spectrum by $\Delta\lambda_{\rm dis}$, which is calibrated using the [O III] λ5007 line. Since the [O III] line is expected to remain constant for much longer timescales (Peterson et al. 2013), we assume that the differences in observed [O III] line widths must be due to small changes in observing and instrumental conditions. For this reason, we also include the observed [O III] emission-line data in our model and calculate the instrumental resolution, $\Delta\lambda_{\rm dis}$, by subtracting the intrinsic [O III] line width, $\Delta\lambda_{\rm true}$, from the observed λ5007 line [O III] line width, $\Delta\lambda_{\rm obs}$, in quadrature:

$$\Delta\lambda_{\rm dis}^2 \approx \Delta\lambda_{\rm obs}^2 - \Delta\lambda_{\rm true}^2. \quad (3)$$

Finally, we note that the description we have outlined above assumes that the response of the emission line to variations in the optical continuum can be approximated as linear around the mean (W22).

3.2. Development of CARAMEL-GAS

The goal of CARAMEL-GAS is to model the BLR gas distribution by including a description of how the gas translates to emission. In general, one could calculate emissivity using photoionization codes such as CLOUDY (Ferland et al. 1998). However, in practice, this complexity would increase the computational power required, and CARAMEL-LIGHT already takes an average of at least 2 weeks to run on supercomputers, per object. Instead, we opt for a simple approximation and describe the BLR surface emissivity, power emitted per unit surface area, as a power law in radial distance, r:

$$\tilde{\epsilon}(r) = \tilde{\epsilon}_0(r/r_0)^{\alpha}, \quad (4)$$

where r represents the BLR radial distance from the central source and $\tilde{\epsilon}(r_0) = \tilde{\epsilon}_0$ is a normalization constant, representing the surface emissivity at a pivot radius r_0 (Robinson 1995; Goad et al. 2012).

In terms of ionizing flux, Equation (4) can be rewritten as

$$\tilde{\epsilon}(\Phi) = \tilde{\epsilon}_0(\Phi/\Phi_0)^{-\alpha/2}. \quad (5)$$

To calculate the emission-line luminosity of particle i from the emissivity (erg s^{-1} cm^{-2}), we assign an emitting size, $A_{c,i}$ to each particle:

$$L_{{\rm line},i}(\lambda) = \tilde{\epsilon}_0(\Phi_i/\Phi_0)^{-\alpha/2}A_{c,i}\delta(\lambda - \lambda_i), \quad (6)$$

where Φ_i is the ionizing flux at the position of particle i. We use a Dirac delta function $\delta(\lambda - \lambda_i)$ to denote the wavelength on the emission line, since the wavelength of the line emission will be determined by the particle's LOS velocity.

Since the ionizing flux is not constant, it can be written as a function of time and the observed continuum, such that

$$\Phi_i = \Phi_i(t) = L_{\rm ion}(t-\tau_i)/4\pi r_i^2, \quad (7)$$

where $L_{\rm ion}(t)$ is the luminosity of the ionizing continuum at time t, $L_{\rm ion}(t-\tau_i)$ is the luminosity of the ionizing continuum that arrives at the particle i at time t given its distance to the ionizing source and associated time delay τ_i, and r_i is the radial distance from the central black hole of particle i, which is determined by the model parameters μ and β.

Combining Equations (6) and (7), the observed line emission luminosity can be written as

$$L_{\rm line}(\lambda, t) = \sum_{i=0}^{N}\tilde{\epsilon}_0\left[\frac{L_{\rm ion}(t-\tau_i)/4\pi r_i^2}{L_{{\rm ion},0}/4\pi r_0^2}\right]^{-\alpha/2}A_{c,i}\delta(\lambda - \lambda_i), \quad (8)$$

where N represents the number of BLR particles surrounding the central source, and the total line emission, $L_{\rm line}(\lambda, t)$, is equal to the sum of the particles' individual line emission. The wavelength, λ, reemitted by particle i is determined by the particle's LOS velocity and the wavelength of the emission line being modeled. The variable r_i is the radial distance from the central black hole of particle i, which is determined by the model parameters μ and β, first introduced in Equation (7), and the variable r_0 is the pivot radius first introduced in Equation (4).

In the initial framework and testing of CARAMEL-GAS done by W22, we assume that all the particles are the same size and define $\epsilon_0 = \tilde{\epsilon}_0 A_c$. We note that we are simply summarizing the initial framework of CARAMEL-GAS here and will be modifying this assumption in Section 3.4 for our sample of 10 AGN.

Equation (8) simplifies to

$$L_{\rm line}(\lambda, t) = \epsilon_0 \sum_{i=0}^{N} \left[\frac{L_{\rm ion}(t-\tau_i)}{L_{\rm ion,0}} \right]^{-\alpha/2} \left[\frac{r_i}{r_0} \right]^{\alpha} \delta(\lambda - \lambda_i). \quad (9)$$

As with CARAMEL-LIGHT, we assume that the BLR response can be approximated as linear around the mean and keep the additive offset, $C_{\rm add}$, to allow the model to match the amplitude of variations in the data. We also use the observed V/B continuum, $L_{\rm obs}(t)$, as a proxy for the ionizing continuum, $L_{\rm ion}(t)$. The emission of each particle is also weighted in the same manner as CARAMEL-LIGHT using the weighting factor W (ξ, ϕ_i, κ) so that the line emission at a given wavelength and time t corresponds to

$$L_{\rm line}(\lambda, t) = \epsilon_0 \sum_{i=0}^{N} \left[\frac{L_{\rm obs}(t-\tau_i) + C_{\rm add}}{L_{\rm obs,0} + C_{\rm add}} \right] \left[\frac{r_i}{r_0} \right]^{\alpha} \times W(\xi, \phi_i, \kappa)\delta(\lambda - \lambda_i), \quad (10)$$

where $L_{\rm obs,0}$ is the mean V/B-band continuum luminosity observed and $L_{\rm obs}(t-\tau_i)$ is the observed V/B continuum luminosity that arrives at a particle at time t given its distance and associated time lag τ_i. The power emitted per unit surface area scales with radial distance from the black hole, r_i, and is determined by the CARAMEL-GAS model parameter, α, which was first introduced in Equation (4).

To minimize covariance, we set the pivot radius, r_0, to the BLR size determined from cross-correlation measurements and the observed luminosity, $L_{\rm obs,0}$, to the mean continuum luminosity of the campaign. We note that we have removed the multiplicative parameter, $C_{\rm mult}$, in the scaling of the line emission since the data used for CARAMEL-GAS are given in luminosity units, rather than the arbitrary fluxes used for CARAMEL-LIGHT modeling.

In summary, the total line emission luminosity is found by summing the contribution of all the particles (Equation (10)), which we have assumed have the same size, and the wavelength of the emission is determined by the particle's LOS velocity. Similar to CARAMEL-LIGHT, we include the observed [O III] λ5007 emission line in our model to calculate instrumental resolution and blur the simulated emission-line profile by $\Delta_{\rm dis}$ (as shown in Equation (3)).

The rest of the CARAMEL geometry and kinematic parameters remain the same; only $C_{\rm mult}$ has been removed, and ϵ_0 and α have been added. Thus, CARAMEL-GAS explores a 28-parameter space, rather than 27 as done in CARAMEL-LIGHT. Here the parameter ϵ_0 represents the emissivity power-law normalization, and the parameter α represents the emissivity power-law index originally introduced in Equation (4).

In addition to the slight change in parameter space, another key difference between the two versions of CARAMEL presented here is that the absolute continuum and spectral fluxes are not modeled in CARAMEL-LIGHT, and instead the fluxes are rescaled so they are in units of order unity. In CARAMEL-GAS, we fit the absolute flux scale of the observed emission lines by ensuring that the input continuum light curves and emission lines are in luminosity units (see Section 3.5 for further details).

3.3. Relevant CARAMEL Model Parameters

As mentioned above, both versions of CARAMEL have over 25 parameters. In addition to the parameters described above in weighting the broad emission line flux via the transparency of the BLR midplane, ξ, and an illumination function, κ, there are other model parameters that provide insight into the geometry and kinematics of the BLR that we would like to highlight here.

A key parameter with any CARAMEL work is the black hole mass constraint given by the model parameter, $\log(M_{\rm bh}/M_{\odot})$. The geometry of the BLR is then given by the inclination angle of the BLR disk, θ_i, and the opening angle (disk thickness), θ_o. In regard to BLR kinematics, we determine the fraction of particles with elliptical orbits via the model parameter $f_{\rm ellip}$, and $1-f_{\rm ellip}$ represents the fraction of particles in either inflowing or outflowing orbits. The parameter $f_{\rm flow}$ ranges from 0 to 1 and determines whether the remaining $1-f_{\rm ellip}$ particles are inflowing or outflowing, with values $f_{\rm flow} < 0.5$ indicating inflow and values $f_{\rm flow} > 0.5$ indicating outflow.

For the purposes of this work, we do not focus on the geometric and kinematic properties of the BLR, as they have all been fully studied in their original CARAMEL-LIGHT studies. For a full review of the BLR geometry and kinematics of each AGN presented in this work, please see their respective CARAMEL-LIGHT paper found in Table 1. Here we are more interested in understanding the BLR gas distribution and further validating the CARAMEL-GAS code. In the following subsection, we describe the minor changes made to CARAMEL-GAS in this work and the testing we will focus on.

3.4. Modifications to CARAMEL-GAS

We note that in our current stages of development one could in principle reparameterize CARAMEL-GAS results to produce CARAMEL-LIGHT results. However, we would like to emphasize that our team's ultimate goal in developing CARAMEL-GAS is to model multiple emission lines simultaneously. Since CARAMEL-LIGHT models the BLR as a Monte Carlo representation of the emissivity field, modeling the BLR of two emission lines does not provide insight into the underlying gas distribution that produces the emission lines. To fit multiple emission lines arising from the same species, i.e., Hα and Hβ, the code must be able to model the BLR as a Monte Carlo representation of the gas density field, which requires additional assumptions about the BLR gas emissivity properties. In this paper, we seek to further test the power law (Equation (4)) implemented in the first version of CARAMEL-GAS, as a step toward modeling the BLR gas distribution with multiple BLR emission lines.

In our initial development and testing of CARAMEL-GAS, we defined a uniform prior for the parameter α, set between values of -2 and 0 (W22). This informed prior was based on the photoionization calculations Goad et al. (2012) computed using CLOUDY models for simple slabs of gas and found $\alpha \sim -1$ for the Hβ emission line. Additionally, we assumed that the BLR particles are all the same size and defined $\epsilon_0 = \tilde{\epsilon}_0 A_c$.

However, of the four emission lines (from three AGN) W22 modeled, CARAMEL-GAS was unable to constrain the parameter α for one, and the remaining three were found to push up against their prior, i.e., preferred less negative solutions. As suggested by W22, pressure models often describe the sizes of BLR clouds as a power law in radial distance from the ionizing source, $A_c(r) \propto r^{\alpha_{\rm size}}$, with $\alpha_{\rm size} \sim 0-1.5$ (Rees et al. 1989). If

we remove our previous assumption in which all BLR particles are the same size, we can consider a more general power law, $\epsilon(r) \propto r^{\alpha}$, such that $\alpha = \alpha_{\rm em} + \alpha_{\rm size}$.

In this work, we build on the initial development and testing of CARAMEL-GAS and allow for a more general power-law index, α, which we now refer to as the radial power-law index. In this way, the radial power-law index α now represents both the emissivity power-law index, $\alpha_{\rm em}$, and the size power-law index of the BLR gas structure/clouds, $\alpha_{\rm size}$.

To determine the line emission at time t with this new generalized radial power-law index, $\alpha = \alpha_{\rm em} + \alpha_{\rm size}$, we go back to Equation (8). Rather than assume that the particles all have the same size, we assume that particles have an emitting size that changes with radius, r, described by a power-law function in radius, such that

$$A_c(r) = A_{c,0}(r/r_0)^{\alpha_{\rm size}}, \tag{11}$$

where r represents the BLR's radial distance from the central source and $A_{c,0} = A_c(r_0)$ is a normalization constant that corresponds to the emitting size of particles at the pivot radius r_0.

We note that in the optically thick limit all absorption and reprocessing of ionized photons will occur at the cloud's surface so that the emitting size, $A_c(r)$, corresponds to the clouds' surface area. In the optically thin limit, however, we expect the relevant emitting size, $A_c(r)$, to be better described by the cloud's volume. In the intermediate, and more realistic, case, we expect the relevant emitting size, $A_c(r)$, to scale in an intermediate way between surface area and volume. Our power law described in Equation (11) holds true for all three scenarios described, as it provides a general description of how the BLR cloud emitting sizes change with radial distance from the ionizing source, regardless of whether the emitting size is best described by a surface area, volume, or some intermediate of the two.

We revisit Equation (8) and update the size of each individual particle, $A_{c,i}$, so that it is described by the power-law function in radial distance, $A_{c,i} = A_c(r_i) = A_{c,0}(r_i/r_0)^{\alpha_{\rm size}}$. Equation (8) now becomes

$$L_{\rm line}(\lambda, t) = \sum_{i=0}^{N} \tilde{\epsilon}_0 \left[\frac{L_{\rm ion}(t - \tau_i)/4\pi r_i^2}{L_{\rm ion,0}/4\pi r_0^2} \right]^{-\alpha_{\rm em}/2} \times A_{c,0} \left(\frac{r_i}{r_0} \right)^{\alpha_{\rm size}} \delta(\lambda - \lambda_i), \tag{12}$$

where $\alpha_{\rm em}$ represents the power-law index for the emissivity power-law function introduced in Equation (4) and $\alpha_{\rm size}$ represents the radial power-law index for the effective size(s) of the BLR structure/clouds introduced in Equation (11).

Since we no longer assume that the BLR particles that represent the gas density field have the same size, we define $\epsilon_0 = \tilde{\epsilon}_0 A_c(r_0) = \tilde{\epsilon}_0 A_{c,0}$ and simplify Equation (12). Doing so allows us to write the line emission at time t as

$$L_{\rm line}(\lambda, t) = \epsilon_0 \sum_{i=0}^{N} \left[\frac{L_{\rm ion}(t - \tau_i)}{L_{\rm ion,0}} \right]^{-\alpha_{\rm em}/2} \left[\frac{r_i}{r_0} \right]^{\alpha_{\rm em} + \alpha_{\rm size}} \times \delta(\lambda - \lambda_i), \tag{13}$$

where, again, $\alpha_{\rm em}$ represents the emissivity power-law index and $\alpha_{\rm size}$ represents the size power-law index of the BLR structure/clouds.

Assuming that the BLR responds linearly to variations in the continuum and using the additive offset, $C_{\rm add}$, as well as the CARAMEL weighting factor $W(\xi, \phi_i, \kappa)$, the total emission line observed from all the model particles can be expressed as

$$L_{\rm line}(\lambda, t) = \epsilon_0 \sum_{i=0}^{N} \left[\frac{L_{\rm obs}(t - \tau_i) + C_{\rm add}}{L_{\rm obs,0} + C_{\rm add}} \right] \left[\frac{r_i}{r_0} \right]^{\alpha} \times W(\xi, \phi_i, \kappa) \delta(\lambda - \lambda_i). \tag{14}$$

Equation (14) is similar to Equation (10), where $L_{\rm obs,0}$ is the mean V/B-band continuum luminosity observed and $L_{\rm obs}(t - \tau_i)$ is the observed V/B continuum luminosity that arrives at a particle at time t given its distance and associated time lag τ_i. Here, however, the radial power-law index parameter, $\alpha = \alpha_{\rm em} + \alpha_{\rm size}$, takes a more generalized form and represents both the emissivity power-law index $\alpha_{\rm em}$, introduced in Equation (4), and the BLR size power-law index $\alpha_{\rm size}$, introduced in Equation (11).

Since we have changed the meaning of the model parameter α, we must also change the parameter's prior. For the contribution from the emissivity power-law index, $\alpha_{\rm em}$, we utilize our previous uniform prior with values between -2 and 0, as we expect negative values from photoionization models (Goad et al. 2012). For the contribution from the size power-law index, $\alpha_{\rm size}$, we use a uniform prior with values between 0 and 1.5 based on pressure law models (Rees et al. 1989). Combining the contributions of both components for the generalized radial power-law index, $\alpha = \alpha_{\rm em} + \alpha_{\rm size}$, we determine a new uniform prior for α with values between -2 and 1.5.

In summary, we have modified CARAMEL-GAS from its initial development to allow the BLR structure to have an effective emitting size that may vary with radial distance from the ionizing source. Since we are expanding both the meaning and prior of the parameter α, we have included the AGN modeled by W22 in the initial development and testing of CARAMEL-GAS, as briefly mentioned in Section 2 above.

3.5. Modeling Details

As previously mentioned, CARAMEL-LIGHT uses normalized continuum and spectral fluxes that are rescaled to units of order unity, while CARAMEL-GAS fits the absolute luminosity scale and thus requires continuum and emission-line data to be in proper luminosity units.

In Table 2, we outline the photometric band used for the continuum light curve of each AGN and whether the data used were measured in flux density units, f_λ (10^{-15} erg cm^{-2} s^{-1} Å^{-1}), or magnitudes. For those measured in magnitudes (i.e., those from the LAMP 2008 campaign), we first convert to flux density units using a B-band zero-point flux of 632×10^{-11} erg cm^{-2} s^{-1} Å^{-1} (Bessell et al. 1998). Once the continuum and Hβ light curves are both in their respective flux density units, we convert to luminosity units using the luminosity distance calculated by adopting a Planck cosmology: $H_0 = 67.8$ km s^{-1} Mpc^{-1}, $\Omega_m = 0.308$, and $\Omega_{\rm vac} = 0.692$ (Planck Collaboration et al. 2016). We choose to adopt this particular cosmology to remain consistent with previous CARAMEL-LIGHT work. The corresponding luminosity distances used for each AGN are found in Column (4) of Table 2.

In addition to testing the generalized radial power-law index that represents both the BLR emissivity and the emitting size

distribution of the BLR structure, $\alpha = \alpha_{\rm em} + \alpha_{\rm size}$, discussed above, we want to further validate CARAMEL-GAS results by directly comparing our results to the published CARAMEL-LIGHT results. In order to provide a fair comparison, we use the same Hβ wavelength range and intrinsic [O III] λ5007 line widths that were used in the initial CARAMEL-LIGHT modeling for our selected sample of 10 AGN (see Columns (5) and (6) in Table 2). We note that the values of the intrinsic [O III] λ5007 line widths used in the initial CARAMEL-LIGHT modeling were determined by converting the FWHM of the line widths presented in Whittle (1992) in units of km s^{-1} to the line dispersion in Å, assuming the Gaussian conversion of 2.35. For objects without a comparison line width by Whittle (1992), we used the median value of the objects in the corresponding campaign (e.g., LAMP 2008, LAMP 2011, LAMP 2016) and a large uncertainty corresponding to $\sim$215 km s^{-1}.

To minimize covariance, we set the pivot radius, r_0, used to calculate the total emission line observed from the model particles (see Equation (14)) to the BLR size determined from cross-correlation measurements, as described in Section 3.2. We tabulate the values used for each AGN, along with the corresponding reference in Table 2. Finally, we include the statistical temperature used to account for systematic uncertainty for using a simple model in Column (8).

3.6. Expected Degeneracies

In this subsection, we discuss some model degeneracies we expect to find in CARAMEL-GAS. First and foremost, we have added an $\alpha_{\rm size}$ component to a more generalized α parameter in this work. Given this general form, the two parameters $\alpha_{\rm em}$ and $\alpha_{\rm size}$ are completely degenerate and cannot be distinguished by our model and data. This degeneracy was first noted by W22, who provided an example of interpreting a value of $\alpha = 0$, given a generalized radial power-law index, $\alpha = \alpha_{\rm em} + \alpha_{\rm size}$. In such a scenario, our model cannot distinguish between two possible solutions: ($\alpha_{\rm em}$, $\alpha_{\rm size}$) = (−1, 1) and ($\alpha_{\rm em}$, $\alpha_{\rm size}$) = (0, 0). The first solution would imply the following: (i) emissivity decreases with increasing radial distance from the ionizing source, in agreement with photoionization models and the work of Goad et al. (2012), and (ii) increasing effective emitting size (s) of the BLR structure/clouds, with radial distance from the ionizing source. The latter, however, would imply that neither emissivity nor the effective emitting size(s) of the BLR structure/clouds change with radial distance. In order to completely rule out one scenario over the other, a greater level of certainty in our understanding of the physics and behavior of the BLR gas is required. We will continue this point of discussion in Section 4 below.

In addition to the degeneracy between the emissivity power-law index, $\alpha_{\rm em}$, and the size power-law index, $\alpha_{\rm size}$, we also expect a degeneracy between the parameter α and the CARAMEL-GAS parameters that describe the radial distribution of particles (μ, β) discussed in Section 3. Here we remind the reader that the parameter β represents the standard deviation of the shifted gamma distribution that describes the radial distribution of particles around the central black hole. Therefore, greater values of β correspond to radial profiles that drop off rapidly with radius. The parameter μ represents the mean value of the shifted gamma distribution, such that greater values of μ translate to radial profiles with larger radii.

Since CARAMEL-GAS models the gas distribution using the Hβ emission observed, the model requires information on how to map the emission to the underlying gas producing the emission, i.e., the simple power law we have chosen (see Equation (14)). Given an emission-line profile, the model can either choose to increase emission at larger radii and have a smaller radius or decrease emission at larger radii and have a larger radius, in order to match the data. For this reason, we expect there to be a degeneracy between the parameters α and μ, as well as the parameters α and β. We will continue our discussion on this expected degeneracy in Section 4.3.3.

4. Results

In this section, we validate CARAMEL-GAS by comparing our results to those found using CARAMEL-LIGHT and present our results for a more generalized radial power-law index, $\alpha = \alpha_{\rm em} + \alpha_{\rm size}$, and possible interpretations.

4.1. CARAMEL-GAS Validation

In general, we do not expect CARAMEL-LIGHT and CARAMEL-GAS to produce identical values, but we do expect model parameters to be in good agreement with one another. As discussed by W22, there are some parameters that are related to the radial distribution of the gas density field that one might expect to change. With a sample of three AGN, W22 showed that these parameters indeed show a slight change, but none were deemed significant.

Here we evaluate six model parameters, $\log(M_{\rm bh}/M_\odot)$, θ_i, θ_o, ξ, κ, and $f_{\rm ellip}$, that are not related to the radial distribution of the gas density field (see Section 3 for description of model parameters). Using the model posteriors from the published CARAMEL-LIGHT results, we compare the median and 68% confidence intervals for the parameters listed above, with our CARAMEL-GAS results in Figure 2. Overall, we see that the model parameters are in general agreement with one another and conclude that the modifications to CARAMEL-GAS produce reliable results. Additionally, the agreement between model parameters also allows us to highlight that despite the simplicity of CARAMEL-LIGHT, in which absolute fluxes are not modeled, the model still results in reliable BLR geometry and kinematics, so long as the results are understood to represent the BLR emissivity field and not the underlying BLR gas density field.

Although our validation has further confirmed the results of CARAMEL-GAS, we would like to reiterate a point made previously by W22: CARAMEL-GAS is not a replacement for CARAMEL-LIGHT. For future work, if black hole mass estimates and insights into the geometry and kinematics of the BLR emissivity are the primary science goals, we still recommend using CARAMEL-LIGHT, since CARAMEL-GAS is still in the early development stages and requires additional assumptions to interpret its results.

4.2. Radial Power-law Index

Now that we have validated the results between CARAMEL-GAS and CARAMEL-LIGHT for our sample of 10 AGN, we can proceed to discuss our results for testing a generalized radial power-law index, $\alpha = \alpha_{\rm em} + \alpha_{\rm size}$.

We present the resulting posterior distribution functions for the radial power-law index, $\alpha = \alpha_{\rm em} + \alpha_{\rm size}$, for the 10 AGN modeled in this work in Figure 3. For readability purposes, we display the results by grouping the AGN with their respective observation campaign, i.e., LAMP 2008, LAMP 2011, or

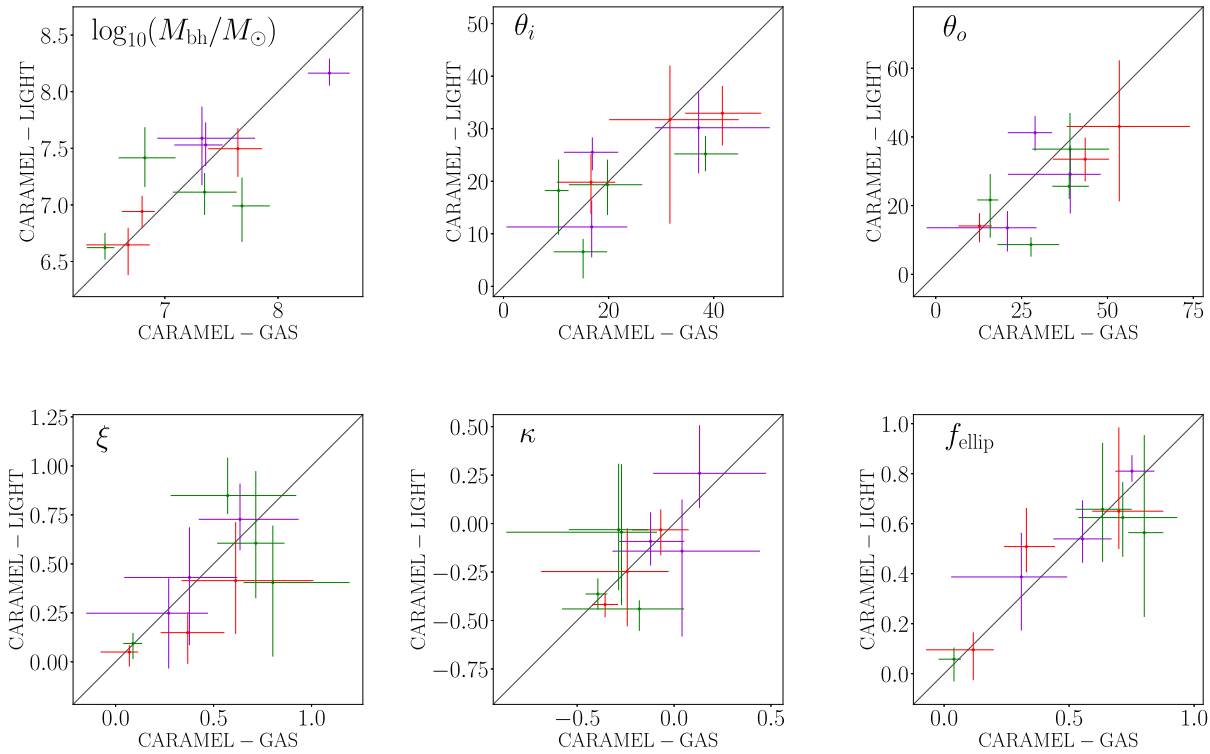

Figure 2. We compare the model parameters determined using both the original version of CARAMEL, CARAMEL-LIGHT, and the results found in this work using CARAMEL-GAS. We chose 6 of the 26 parameters the codes have in common to compare. On the *x*-axis of each plot, we depict the CARAMEL-GAS results found in this work, and on the *y*-axis of each plot, we show the previously published results found using CARAMEL-LIGHT. From left to right: the top panels show results for black hole mass, $\log(M_{\rm bh}/M_\odot)$, inclination angle, θ_i, and opening angle (disk thickness), θ_o; the bottom panels show midplane transparency, ξ, the illumination factor, κ, and the fraction of particles on elliptical orbits, $f_{\rm ellip}$. The colored circles and error bars show the median and 1D 68% confidence interval of the 2D posterior PDFs for each AGN. The solid black line represents an exact match in results. Purple points are for the AGN from LAMP 2016, red points are from LAMP 2011, and green points are from LAMP 2008. Overall we see that our CARAMEL-GAS and CARAMEL-LIGHT results are in good agreement.

LAMP 2016. We also tabulate these results in Table 3 and report the median value and 68% confidence interval. Looking at the posteriors in Figure 3, we find the best converged results for the LAMP 2016 campaign and note that the models for Mrk 1310 and SBS 1116+584A (LAMP 2008) were unable to constrain the α parameter.

4.3. Possible Interpretations

In general, we find that our models prefer positive values for $\alpha = \alpha_{\rm em} + \alpha_{\rm size}$. As expected, with the modifications we have made to CARAMEL-GAS in this work, we are not able to distinguish between the radial emissivity power-law index, $\alpha_{\rm em}$, and the radial size power-law index, $\alpha_{\rm size}$, as previously discussed in Section 3.6. However, we can still speculate about the different possible interpretations and physical scenarios in which a positive radial power-law index, $\alpha = \alpha_{\rm em} + \alpha_{\rm size} > 0$, would be favored.

4.3.1. BLR Structure/Cloud Size Distribution

Based on photoionization models, we might expect BLR emissivity to decrease with radial distance from the ionizing source and thus a negative emissivity power-law index, $\alpha_{\rm em}$. Under this assumption, we can deduce that a value of $\alpha_{\rm em} \sim -1$ or $\alpha_{\rm em} \sim -2$ is expected, and CLOUDY models suggest $\alpha_{\rm em} \sim -1$ for Hβ slabs of gas (Goad et al. 2012).

If we assume $\alpha_{\rm em} \sim -2$, then our CARAMEL-GAS models, which favor a positive $\alpha = \alpha_{\rm em} + \alpha_{\rm size} > 0$, imply $\alpha_{\rm size} \gtrsim 2$. In such a case, we might imagine that the BLR is composed of discrete clouds that increase in effective emitting size as a function of radial distance squared and get increasingly larger the farther away they are from the black hole. In the more likely case, as suggested by photoionization calculations, in which

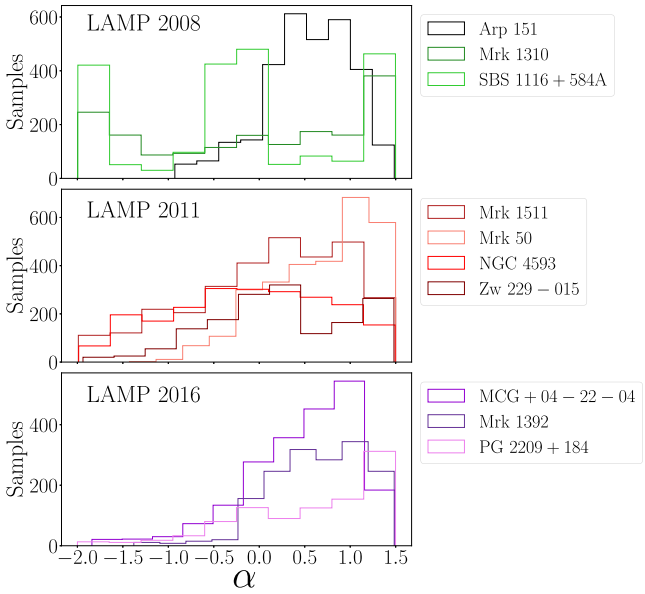

Figure 3. The posterior distribution functions of the generalized radial power-law index parameter, $\alpha = \alpha_{\rm em} + \alpha_{\rm size}$, are shown above. The results are split up by campaign. The top panel represents AGN in our sample that were observed during the LAMP 2008 campaign, the middle panel represents AGN in our sample that were observed during the LAMP 2011 campaign, and the bottom panel represents AGN in our sample that were observed during the LAMP 2016 campaign.

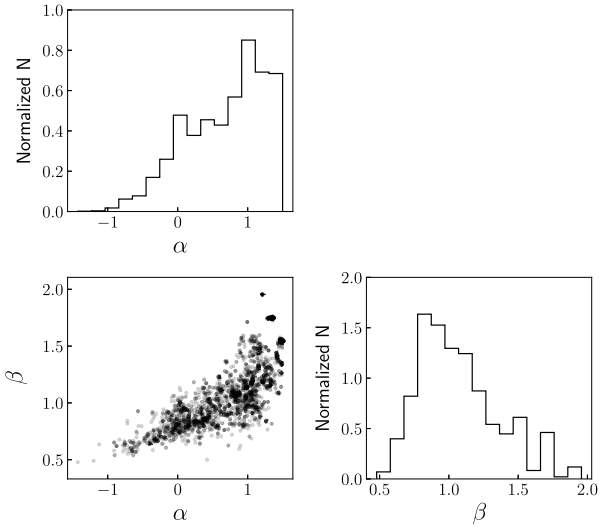

Figure 4. Selected posterior plots for Mrk 50 from the LAMP 2011 sample. Bottom left: the 2D posterior plot between model parameters α and β, with α on the x-axis and β on the y-axis. The 2D posterior plot shows covariance between the model parameters, such that positive values of α are correlated with greater values of β and negative values of α are correlated with smaller values of β. Since increasing values of β correspond to radial profiles that drop off rapidly, the model can choose to have either rapid radial drop-offs that are offset by positive values of α, i.e., placing emission at the outer edges, or smaller values of β (i.e., larger BLR radius) accompanied by negative values of α so that emission decreases with radius, given the larger BLR radius. Top left: 1D posterior plot of the parameter α. Bottom right: 1D posterior plot of the parameter β.

$\alpha_{\rm em} \sim -1$, our models imply $\alpha_{\rm size} \geqslant 1$, and the BLR clouds only slightly increase in effective emitting size with increasing radial distance, in a linear manner.

If we accept that our CARAMEL-GAS Monte Carlo representation of the gas density field implies a picture of BLR clouds with increasing emitting sizes as a function of radial distance, the question of a physical description follows. One possible description we propose is that a decrease in radiation pressure with radial distance leads to a decrease in the density of the BLR gas, and consequently an increase in size with increasing radial distance from the ionizing source, such that the emitting size(s) of the BLR structure/clouds increase with radial distance. Alternatively, we suggest tidal forces as another possible explanation. Since tidal forces will be greater at a closer proximity to the central black hole, this could lead to fragmentation of the BLR structure/clouds closer to the inner edges of the BLR disk. This would cause the clouds at farther radial distances to appear to have larger sizes since they have not experienced as much fragmentation. Finally, we propose that the clouds at smaller radial distances might be sheared by differential rotation, in which case clouds at larger radial distances that do not experience shearing appear to have greater effective emitting sizes.

4.3.2. BLR Emissivity Distribution

Since we cannot distinguish between $\alpha_{\rm size}$ and $\alpha_{\rm em}$ in our model, we cannot completely rule out the interpretation in which our results of a positive $\alpha = \alpha_{\rm em} + \alpha_{\rm size} > 0$ actually correspond to positive values of $\alpha_{\rm em}$. In this scenario, we assume that the Monte Carlo representation of the gas density field is not a description of discrete clouds, but rather a dynamic windlike structure, such that $\alpha_{\rm size} = 0$.

Table 3
Radial Power-law Index, α

Campaign	Galaxy	α
LAMP 2008 (P14)	Arp 151	$0.57^{+0.46}_{-0.45}$
	Mrk 1310	$0.08^{+1.67}_{-1.19}$
	SBS 1116+583A	$-0.21^{+1.59}_{-1.44}$
LAMP 2011 (W18)	Mrk 1511	$0.21^{+1.06}_{-0.75}$
	Mrk 50	$0.81^{+0.79}_{-0.45}$
	NGC 4593	$-0.09^{+0.99}_{-0.94}$
	Zw 229-015	$0.18^{+0.73}_{-1.00}$
LAMP 2016 (V22)	MCG +04-22-042	$0.61^{+0.72}_{-0.46}$
	Mrk 1392	0.66 ± 0.54
	PG 2209+184	$0.73^{+0.99}_{-0.63}$

Note. The best fit for the generalized radial power-law index, $\alpha = \alpha_{\rm em} + \alpha_{\rm size}$, which represents both a radial emissivity power-law index and a radial size power-law index. Column (1) specifies the corresponding campaign and original published CARAMEL-LIGHT work of the AGN found in Column (2). Column (3) shows the median value of the model fit and 68% confidence interval.

If $\alpha_{\rm size} = 0$, then positive values of $\alpha = \alpha_{\rm em} + \alpha_{\rm size}$ imply $\alpha_{\rm em} > 0$, such that BLR emission is concentrated at the edges, or increases with radial distance from the ionizing source. This scenario could be possible if parts of the BLR closer to the plane of the accretion disk are optically thick, perhaps due to a bowl-shape geometry, such as the one suggested by Goad et al. (2012). In this picture, the inner regions of the bowl are less reflective, and emissivity thus increases at greater radial distances. Additionally, in the case of an optically thick BLR, we might expect larger covering factors closer to the ionizing source, so that greater fractions of the continuum are absorbed by the BLR, as seen from the central engine. In this scenario, the covering factor decreases with radial distance from the central source, allowing for more emission at larger radial distances. Another physical description that could lead to emission at the edges of the BLR is self-shadowing within the BLR disk at inner radii by gas at larger radii, similar to that suggested for the accretion disk by Wang et al. (2012).

4.3.3. Better Theoretical Input Needed

The discussion in Sections 4.3.1 and 4.3.2 shows that in order to constrain the underlying BLR gas distribution from reverberation mapping data, our models need a more informative picture of how BLR emission maps to gas density. Qualitatively, this is intuitive and expected. We are now in the position to quantify these degeneracies and formulate more specific requirements from theoretical models.

Returning to the expected degeneracies between the model parameters α and β and the model parameters α and μ first discussed in Section 3.6, we look at the 2D posterior plots of α and β (Figure 4) and α and μ (Figure 5) for Mrk 50. The 2D posterior plots for the rest of our sample can be found in Figures 6–12 in the Appendices.

As seen in the bottom left panel of Figure 4, we see covariance between the model parameters α and β, such that positive values of α are correlated with greater values of β and negative values of α are correlated with smaller values of β. Since increasing values of β correspond to radial profiles that drop off rapidly, the model can choose to have either rapid

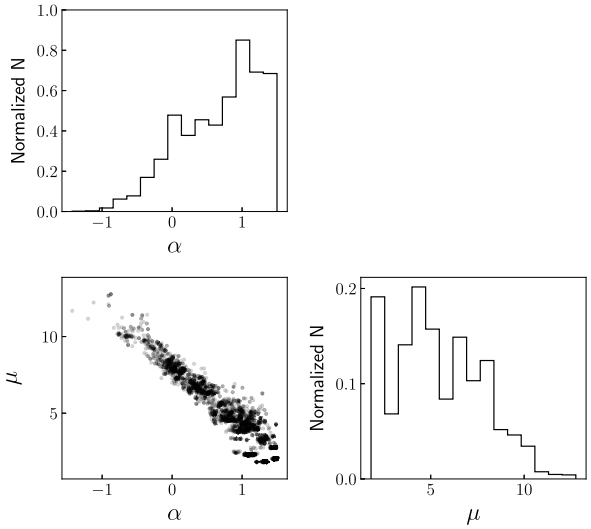

Figure 5. Selected posterior plots for Mrk 50 from the LAMP 2011 sample. Bottom left: the 2D posterior plot between model parameters α and μ, with α on the x-axis and μ on the y-axis. The 2D posterior plot shows covariance between the model parameters, such that positive values of α are correlated with smaller values of μ and negative values of α are correlated with larger values of μ. Since increasing values of μ correspond to radial profiles with larger radii, the model can choose to have either a larger BLR radius that is accompanied by negative values of α, i.e., decreased emission with radius, or smaller values of μ (i.e., smaller BLR radius) that are offset with positive values α so that emission increases with radius, given the smaller BLR radius. Top left: 1D posterior plot of the parameter α. Bottom right: 1D posterior plot of the parameter μ.

radial drop-offs (smaller BLR radii) that are offset by positive values of α (placing emission at the outer edges) or smaller values of β (larger BLR radii) accompanied by negative values of α, so that emission decreases with radius, given the larger BLR radius.

Similarly, looking at the bottom left panel of Figure 5, the covariance between the model parameters α and μ exists, such that positive values of α are correlated with smaller values of μ and negative values of α are correlated with larger values of μ. Since increasing values of μ correspond to radial profiles with larger radii, the model can choose to have either a larger BLR radius that is accompanied by negative values of α (decreased emission with radius) or smaller values of μ (smaller BLR radii) that are offset with positive values α, so that emission increases with radius, given the smaller BLR radius.

In both cases, the model is choosing between (i) a larger BLR radius (as described by smaller values of β or larger values of μ) with decreasing emission as a function of radius ($\alpha < 0$) and (ii) a smaller BLR radius (as described by larger values of β or smaller values of μ) with increasing emission as a function of radius ($\alpha > 0$). The latter could be due to either emission at the outer edges of the BLR structure due to geometric effects ($\alpha_{\rm em} > 0$) or larger cloud sizes ($\alpha_{\rm size} > 0$) as previously discussed. For this reason, we conclude that our models need more physically motivated priors before we can proceed with empirical modeling of the BLR gas distribution.

5. Conclusion

In this work, we expanded on the initial development of CARAMEL-GAS, which models the BLR gas density field using reverberation mapping data. The first version of the code used a simple power law to describe the emissivity of the gas, and early tests indicated that models might prefer values greater than zero. Here we introduced a more general power law, $\alpha = \alpha_{\rm em} + \alpha_{\rm size}$, which also considers the effective emitting size(s) of the BLR structure/clouds, via $\alpha_{\rm size}$. Using a sample of 10 AGN observed during three different LAMP campaigns, and previously modeled with CARAMEL-LIGHT, we tested the general power-law index, $\alpha = \alpha_{\rm em} + \alpha_{\rm size}$, and compared our geometry and kinematic model results with those determined by CARAMEL-LIGHT.

Overall, we find that CARAMEL-LIGHT and CARAMEL-GAS results are in general agreement, adding to the body of evidence supporting that black hole masses and other key parameters derived from this method are robust. We continue to recommend the use of the original version of the code, CARAMEL-LIGHT, for estimating black hole mass and studying the structure and kinematics of the BLR emissivity.

We find that positive values of a generalized radial power-law index ($\alpha_{\rm em} + \alpha_{\rm size} > 0$) are preferred, and we provide the following interpretations: (i) If we assume $\alpha_{\rm em} < 0$, then $\alpha_{\rm size} > 0$, which implies that the effective emitting size(s) of the BLR structure/clouds must increase as a function of radial distance from the central black hole, perhaps due to increasing tidal forces or shearing from differential rotation at inner radii, or even a decrease in radiation pressure at larger radii. (ii) Alternatively, if we assume $\alpha_{\rm size} = 0$, then $\alpha_{\rm em} > 0$ implies that emission is concentrated at the edges, perhaps due to a BLR disk that is optically thick at inner radii. In this scenario, we suggest larger cover factors closer to the ionizing source, a bowl-shaped geometry with inner regions that are less reflective, or even self-shadowing of the inner BLR disk by the outer BLR disk.

We believe that empirical modeling of the BLR gas distribution requires further insight into which of these two scenarios described above is physically motivated and preferred, in order to provide CARAMEL-GAS with more informative prior knowledge.

Acknowledgments

We thank the anonymous referee for helpful comments and suggestions, which significantly improved this manuscript. L.V. and T.T. gratefully acknowledge support from the NSF through grant AST-1907208, "Collaborative Research: Establishing the Foundations of Black Hole Mass Measurements of AGN across Cosmic Time." V.N.B. gratefully acknowledges assistance from the NSF through grant AST-1909297. Note that findings and conclusions do not necessarily represent views of the NSF.

V.U. acknowledges partial funding support from NASA Astrophysics Data Analysis Program (ADAP) grant Nos. 80NSSC20K0450 and 80NSSC23K0750 and STScI grant Nos. HST-AR-17063.005-A, HST-GO-17285.001-A, and JWST-GO-01717.001-A.

Appendix

In the paper, we discuss the expected degeneracy between the model parameters α, β, and μ and highlight the 2D posterior plots of Mrk 50 from the LAMP 2011 sample. Here, we provide the 2D posterior plots for the rest of the AGN in our sample in Figures 6–12 in Appendices A–G. We excluded Mrk 1310 and SBS 1116+583A from the LAMP 2008 sample, however, since the models were unable to constrain the α parameter.

Appendix A
Arp 151 (LAMP 2008)

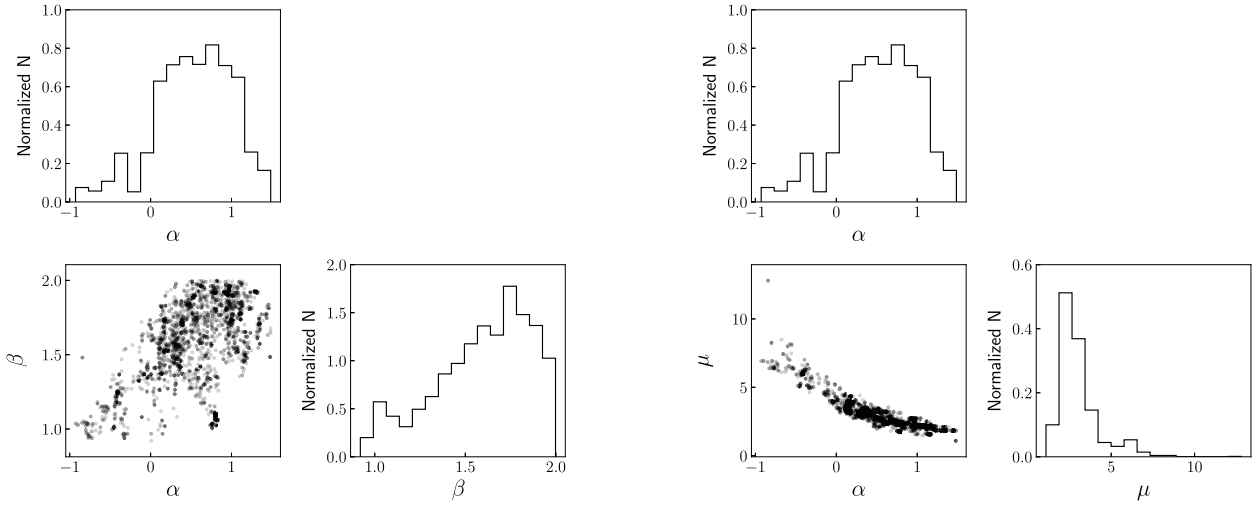

(a) α vs β (b) α vs μ

Figure 6. (a) Bottom left: the 2D posterior plot between model parameters α and β, with α on the *x*-axis and β on the *y*-axis. The 2D posterior plot shows covariance between the model parameters, such that positive values of α are correlated with greater values of β and negative values of α are correlated with smaller values of β. Since increasing values of β correspond to radial profiles that drop off rapidly, the model can choose to have either rapid radial drop-offs that are offset by positive values of α, i.e., placing emission at the outer edges, or smaller values of β (i.e., larger BLR radius) accompanied by negative values of α so that emission decreases with radius, given the larger BLR radius. Top left: 1D posterior plot of the parameter α. Bottom right: 1D posterior plot of the parameter β. (b) Bottom left: the 2D posterior plot between model parameters α and μ, with α on the *x*-axis and μ on the *y*-axis. The 2D posterior plot shows covariance between the model parameters, such that positive values of α are correlated with smaller values of μ and negative values of α are correlated with larger values of μ. Since increasing values of μ correspond to radial profiles with larger radii, the model can choose to have either a larger BLR radius that is accompanied by negative values of α, i.e., decreased emission with radius, or smaller values of μ (i.e., smaller BLR radius) that are offset with positive values α so that emission increases with radius, given the smaller BLR radius. Top left: 1D posterior plot of the parameter α. Bottom right: 1D posterior plot of the parameter μ.

Appendix B
Mrk 1511 (LAMP 2011)

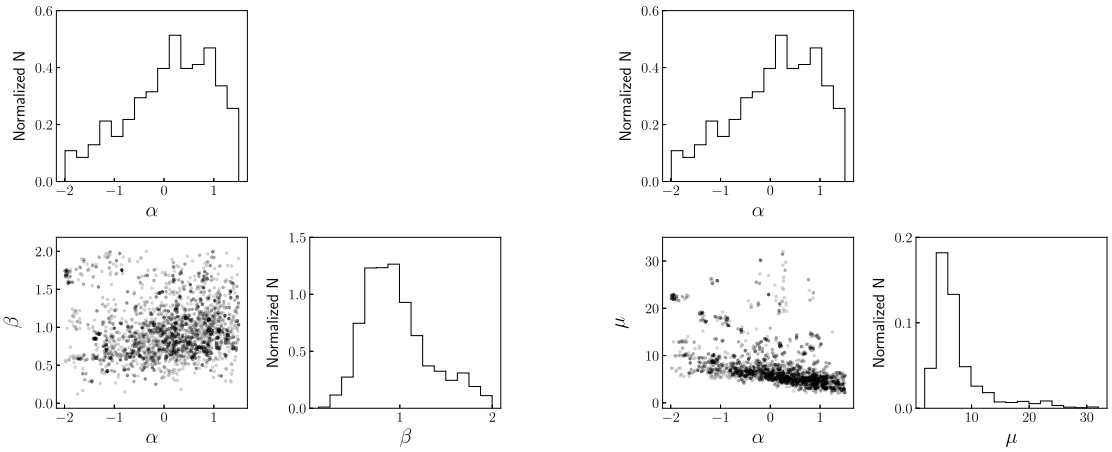

(a) α vs β (b) α vs μ

Figure 7. Same as Figure 6, but for Mrk 1511.

Appendix C
NGC 4593 (LAMP 2011)

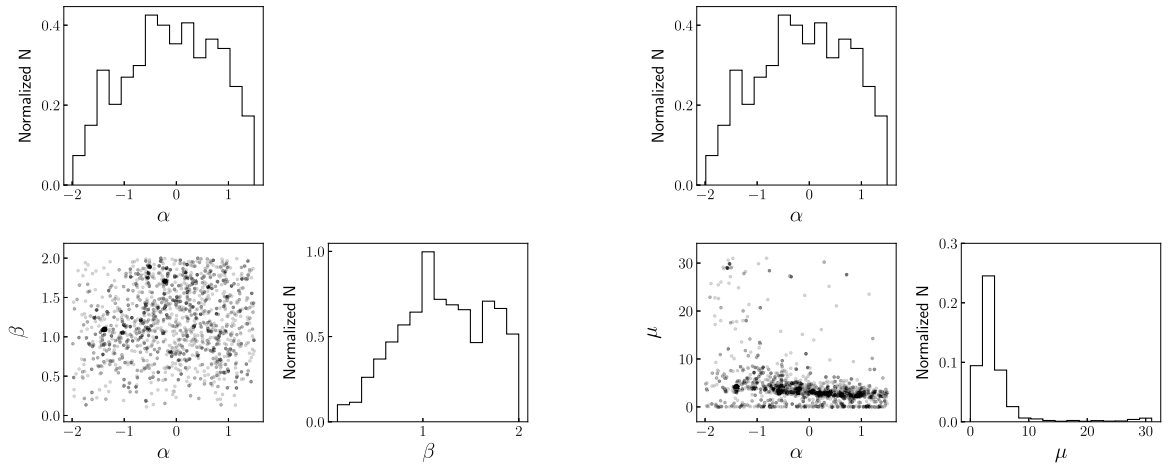

(a) α vs β (b) α vs μ

Figure 8. Same as Figure 6, but for NGC 4593.

Appendix D
Zw 229-015 (LAMP 2011)

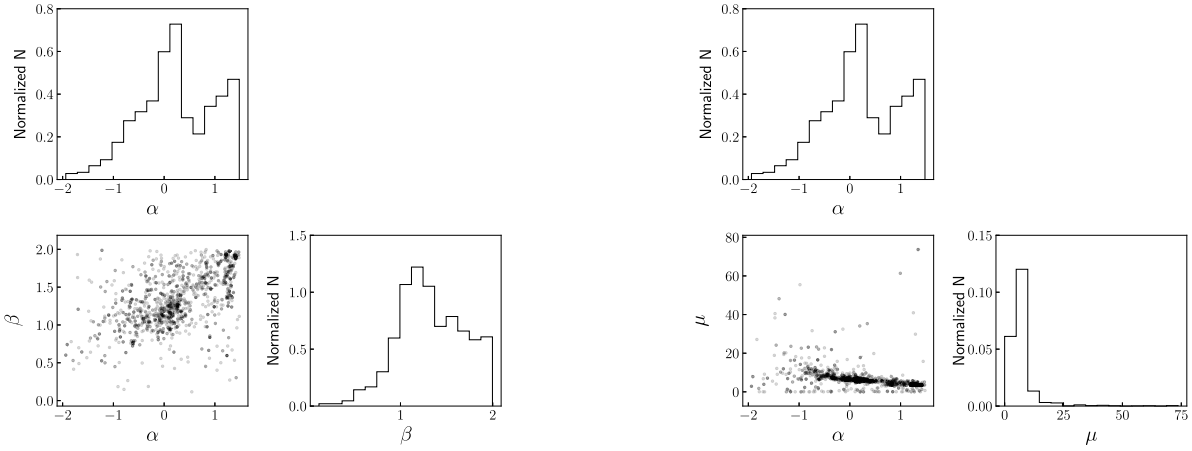

(a) α vs β (b) α vs μ

Figure 9. Same as Figure 6, but for Zw 229-015.

Appendix E
MCG +04-22-042 (LAMP 2016)

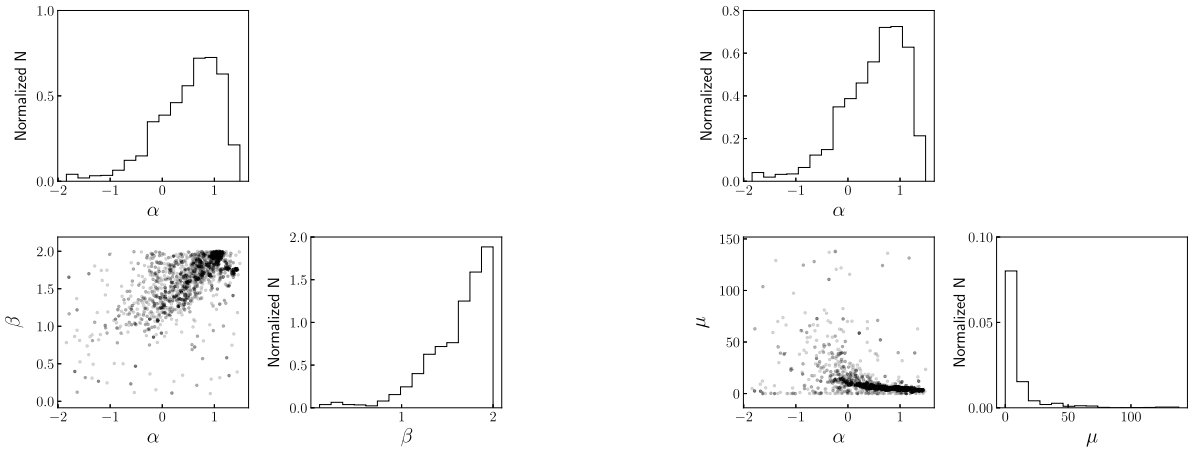

(a) α vs β (b) α vs μ

Figure 10. Same as Figure 6, but for MCG +04-22-042.

Appendix F
Mrk 1392 (LAMP 2016)

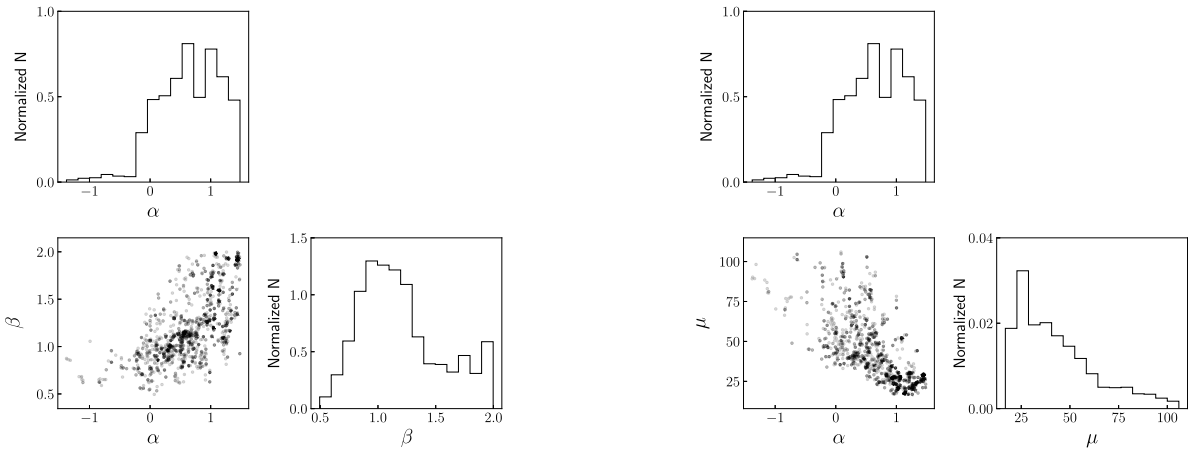

(a) α vs β (b) α vs μ

Figure 11. Same as Figure 6, but for Mrk 1392.

Appendix G
PG 2209+184 (LAMP 2016)

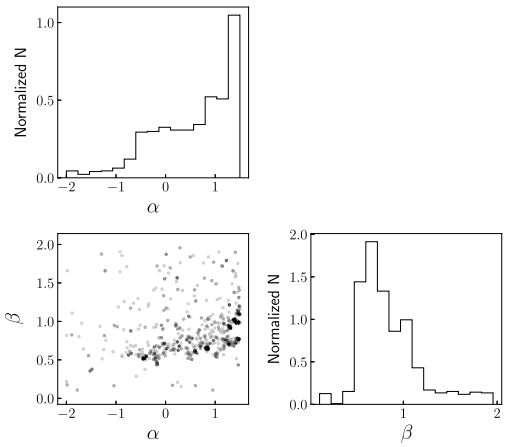

(a) α vs β

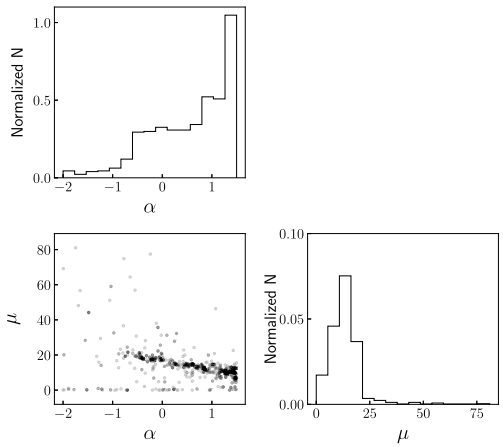

(b) α vs μ

Figure 12. Same as Figure 6, but for PG 2209+184.

ORCID iDs

Lizvette Villafaña https://orcid.org/0000-0002-1961-6361
Tommaso Treu https://orcid.org/0000-0002-8460-0390
Lourenzo Colleyn https://orcid.org/0009-0002-3013-7131
Aaron J. Barth https://orcid.org/0000-0002-3026-0562
Matthew A. Malkan https://orcid.org/0000-0001-6919-1237
Vivian U https://orcid.org/0000-0002-1912-0024
Vardha N. Bennert https://orcid.org/0000-0003-2064-0518

References

Antonucci, R. 1993, ARA&A, 31, 473
Baldwin, J., Ferland, G., Korista, K., & Verner, D. 1995, ApJL, 455, L119
Barth, A. J., Bennert, V. N., Canalizo, G., et al. 2015, ApJS, 217, 26
Barth, A. J., Nguyen, M. L., Malkan, M. A., et al. 2011, ApJ, 732, 121
Bentz, M. C., & Katz, S. 2015, PASP, 127, 67
Bentz, M. C., Markham, M., Rosborough, S., et al. 2023a, ApJ, 959, 25
Bentz, M. C., Onken, C. A., Street, R., & Valluri, M. 2023b, ApJ, 944, 29
Bentz, M. C., Street, R., Onken, C. A., & Valluri, M. 2021a, ApJ, 906, 50
Bentz, M. C., Walsh, J. L., Barth, A. J., et al. 2009, ApJ, 705, 199
Bentz, M. C., Williams, P. R., Street, R., et al. 2021b, ApJ, 920, 112
Bentz, M. C., Williams, P. R., & Treu, T. 2022, ApJ, 934, 168
Bessell, M. S., Castelli, F., & Plez, B. 1998, A&A, 333, 231
Blandford, R. D., & McKee, C. F. 1982, ApJ, 255, 419
Booth, C. M., & Schaye, J. 2009, MNRAS, 398, 53
Brewer, B. J., & Foreman-Mackey, D. 2018, J. Stat. Software, 86, 1
Cackett, E. M., Bentz, M. C., & Kara, E. 2021, iSci, 24, 102557
Cackett, E. M., & Horne, K. 2006, MNRAS, 365, 1180
De Rosa, G., Peterson, B. M., Ely, J., et al. 2015, ApJ, 806, 128
Dubois, Y., Peirani, S., Pichon, C., et al. 2016, MNRAS, 463, 3948
Elvis, M., Marengo, M., & Karovska, M. 2002, ApJL, 567, L107
Emmering, R. T., Blandford, R. D., & Shlosman, I. 1992, ApJ, 385, 460
Fabian, A. C. 2012, ARA&A, 50, 455
Ferland, G. J., Korista, K. T., Verner, D. A., et al. 1998, PASP, 110, 761
Goad, M. R., Korista, K. T., & Ruff, A. J. 2012, MNRAS, 426, 3086
Gravity Collaboration, Amorim, A., Bauböck, M., et al. 2020, A&A, 643, A154
Gravity Collaboration, Amorim, A., Bauböck, M., et al. 2021, A&A, 648, A117
Gravity Collaboration, Sturm, E., Dexter, J., et al. 2018, Natur, 563, 657
Grier, C. J., Pancoast, A., Barth, A. J., et al. 2017, ApJ, 849, 146
Horne, K. 1994, in ASP Conf. Ser. 69, Reverberation Mapping of the Broad-Line Region in Active Galactic Nuclei, ed. P. M. Gondhalekar, K. Horne, & B. M. Peterson (San Francisco, CA: ASP), 23
Kara, E., Mehdipour, M., Kriss, G. A., et al. 2021, ApJ, 922, 151
Kartje, J. F., & Königl, A. 1996, VA, 40, 133
Kaspi, S., Smith, P. S., Netzer, H., et al. 2000, ApJ, 533, 631
Kishimoto, M., Hönig, S. F., Antonucci, R., et al. 2011, A&A, 536, A78
Konigl, A., & Kartje, J. F. 1994, ApJ, 434, 446
Koshida, S. 2015, TORUS2015: The AGN Unification Scheme after 30 Years, ed. P. Gandhi & S. F. Hoenig,
Krolik, J. H. 1988, ApJ, 325, 148
Li, Y.-R., Wang, J.-M., Ho, L. C., Du, P., & Bai, J.-M. 2013, ApJ, 779, 110
Maiolino, R., Risaliti, G., Salvati, M., et al. 2010, A&A, 517, A47
Mangham, S. W., Knigge, C., Matthews, J. H., et al. 2017, MNRAS, 471, 4788
Murray, N., Chiang, J., Grossman, S. A., & Voit, G. M. 1995, ApJ, 451, 498
Netzer, H. 2015, ARA&A, 53, 365
Pancoast, A., Brewer, B. J., Treu, T., et al. 2014, MNRAS, 445, 3073
Peterson, B. M. 1993, PASP, 105, 247
Peterson, B. M. 2006, in Physics of Active Galactic Nuclei at All Scales, ed. D. Alloin, R. Johnson, & P. Lira, 693 (Berlin: Springer), 77
Peterson, B. M., Denney, K. D., De Rosa, G., et al. 2013, ApJ, 779, 109
Peterson, B. M., Ferrarese, L., Gilbert, K. M., et al. 2004, ApJ, 613, 682
Planck Collaboration, Ade, P. A. R., Aghanim, N., et al. 2016, A&A, 594, A13
Rees, M. J., Netzer, H., & Ferland, G. J. 1989, ApJ, 347, 640
Robinson, A. 1995, MNRAS, 272, 647
Rosborough, S., Robinson, A., & Almeyda, T. 2023, AAS Meeting, 55, 137.02D
Scoville, N., & Norman, C. 1988, ApJ, 332, 163
Somerville, R. S., & Davé, R. 2015, ARA&A, 53, 51
U, V., Barth, A. J., Vogler, H. A., et al. 2022, ApJ, 925, 52
Urry, C. M. 2003, BAAS, 35, 726
Urry, C. M., & Padovani, P. 1995, PASP, 107, 803
Villafaña, L., Williams, P. R., Treu, T., et al. 2022, ApJ, 930, 52
Walsh, J. L., Minezaki, T., Bentz, M. C., et al. 2009, ApJS, 185, 156
Wang, Y., Ferland, G. J., Hu, C., Wang, J.-M., & Du, P. 2012, MNRAS, 424, 2255
Waters, T., Kashi, A., Proga, D., et al. 2016, ApJ, 827, 53
Waters, T., & Li, H. 2019, arXiv:1912.03382
Whittle, M. 1992, ApJS, 79, 49
Williams, P. R., Pancoast, A., Treu, T., et al. 2018, ApJ, 866, 75
Williams, P. R., Pancoast, A., Treu, T., et al. 2020, ApJ, 902, 74
Williams, P. R., & Treu, T. 2022, ApJ, 935, 128